JOURNAL OF AIRCRAFT
Vol. 44, No. 4, July–August 2007

Magnetometer Autocalibration Leveraging Measurement Locus Constraints

Demoz Gebre-Egziabher*
University of Minnesota, Twin Cities, Minneapolis, Minnesota 55455

DOI: 10.2514/1.27118

An autocalibration algorithm for calibration of magnetometer triads used to determine heading in small aerial vehicles is developed and its performance is analyzed. The algorithm estimates the 12 calibration parameters, which are elements of an affine transformation mapping measured, and thus, erroneous magnetometer measurements into corrected field measurements. The mapping corrects magnetometer output errors due to hard-iron biases, scale factor deviations, and nonorthogonality effects caused by soft irons or physical arrangement of the sensor axes. The correction mapping is determined by leveraging the fact that the locus of Earth's magnetic field vector as measured by a triad of magnetometers is an ellipsoid. The coefficients defining the ellipsoid are computed using a total least-squares estimator. It is shown that, generally, in such autocalibration algorithms, soft-iron errors and sensing axes nonorthogonality can result in an error mode that is unobservable. These conditions are identified and the algorithm incorporates a method for detecting them. In these instances, even though autocalibration can provide an estimate of only 9 of the 12 calibration parameters, it is shown that how external measurements from a triad of accelerometers and a global positioning system receiver can provide the information needed to estimate the unobservable error mode.

Nomenclature

$\boldsymbol{b}$	=	hard-iron bias vector
$\boldsymbol{h}$	=	Earth's magnetic field vector (true value)
$\boldsymbol{h}^b$	=	Earth's magnetic field vector (true body axes value)
$\boldsymbol{h}^m$	=	Earth's magnetic field vector (measured value)
$\mathbf{I}_{n\times n}$	=	$n \times n$ identity matrix
$\boldsymbol{n}$	=	wide band (sampling) noise on vector
s_i	=	i axis magnetometer scale factor error
$\mathbf{U}_C$	=	matrix of the left eigenvector of matrix $\mathbf{C}$
$\mathbf{V}_C$	=	matrix of the right eigenvector of matrix $\mathbf{C}$
α_{ij}	=	soft iron/magnetic induction coefficient ij
η_i	=	i axis misalignment angle
Σ_C	=	matrix (diagonal) of singular values for the matrix $\mathbf{C}$

Introduction

MAGNETOMETERS are devices that measure the strength of magnetic fields and are used extensively in navigation, guidance, and control applications. In aircraft and marine navigation, for example, they are used as heading sensors. In satellite guidance and control applications they are used as attitude sensors. In these applications, the magnetometers are used to measure components of Earth's magnetic field vector from which vehicle heading or attitude is deduced. Because their output is corrupted by errors, magnetometers are normally calibrated before they are used. The calibration process involves estimating the magnetometer output errors and using these estimates to correct subsequent magnetometer measurements. In general, magnetometer output errors are caused by random wide band noise, constant biases or null shifts, time-varying biases arising from magnetic induction, scale factor deviations, sensor-to-vehicle axes misalignments, and nonorthogonality of the sensor axes.

The environment around magnetometers in a vehicle affects the nature of some of these the output errors. Magnetically hard materials in the vicinity of the magnetometers, for example, add a constant null shift or bias to the sensor output. Magnetically soft materials interact with Earth's magnetic field and generate biases that change as the vehicle's orientation relative to the local magnetic field changes. Constant biases or null shifts caused by magnetically hard materials are sometimes referred to as hard-iron biases, whereas biases due to magnetic induction from magnetically soft materials are called soft-iron errors [1,2].

The magnetic environment in the vicinity of magnetometers is not a constant and can change as a function of time. This change can occur, for example, after maintenance on or near to the magnetometers. In small aerial vehicles lacking a dedicated avionics bay separated by some distance from the vehicle's payload, this change can be severe; the magnetic environment around the sensors can be different from one flight to the next depending on what payload is on board a particular flight. Thus, it is normal to perform magnetometer calibrations in situ to account for the magnetic environment around the sensor.

The work in this paper is concerned with developing autocalibration algorithms for magnetometer triads used for heading determination in small aircraft in the category of micro aerial vehicles (MAVs). In these applications cost considerations preclude the use of high accuracy rate gyros for heading and attitude determination. Even though there are systems that generate an attitude solution by fusing the information from low-cost-rate gyros, accelerometers, and global positioning system (GPS) [3], these systems are known to be conditionally observable in that heading errors can be kept in check only as long as the vehicle is experiencing accelerations [4–8]. Thus, magnetometers are one of the sensors of choice for heading determination or a means by which to arrest the growth of the heading solution computed by inertial sensors [9,10].

Background

The literature discussing in situ calibration algorithms for magnetometers used in satellites is extensive. Some of these algorithms rely on the fact that Earth's magnetic field vector is a well-known function of position [11]. Thus, given that a vehicle is at a known location, Earth's magnetic field vector can be resolved into a coordinate frame attached to the vehicle. A comparison between the resolved magnetic field vector and the measurement from the magnetometers is used to calibrate the sensors [12]. These algorithms require that the orientation of the vehicle be known a priori. This can

Received 7 August 2006; revision received 18 February 2007; accepted for publication 18 February 2007.

*Assistant Professor, Department of Aerospace Engineering and Mechanics.

be problematic unless the vehicle has an attitude determination system that does not rely on the magnetometers.

A class of algorithms known as "attitude-free" algorithms obviate the need for knowledge of the vehicle's orientation during calibration [13–15]. They leverage the diversity of Earths's magnetic field vector as a function of location. That is, samples of Earth's magnetic field taken at geographically diverse location are used to estimate magnetometer calibration parameters. These algorithms can be called autocalibration algorithms because the primary inputs into the calibration algorithm are the measured (or erroneous) magnetometer measurements.

There is another class of algorithms that can be classified as semi-attitude-free algorithms and are similar to the ones developed and analyzed in this paper. These algorithms have been used in satellite [16–19] and virtual reality [20,21] applications. They use the magnitude of Earth's magnetic field vector in a given location as a constraint to perform an autocalibration: a calibration without the need of any information beyond the magnetometer outputs themselves. However, as was shown in [17] and will be discussed more detail here, there can be an unobservable mode in these calibration algorithms. In these cases, they are not autocalibration algorithms and will require external (although minimal) information to complete the calibration.

Unlike the magnetometers used in satellite applications, the literature discussing algorithms suitable for calibrating magnetometers used in heading or attitude determination in small aerial vehicles (or vehicles operating close to the surface of Earth) is not extensive. Examples include the algorithms discussed in [22,23], which can be thought of aviation analogs of the marine compass swinging algorithms discussed in [24,25]. These are algorithms suited for magnetometer pairs or floated magnetic compasses (i.e., compasses with a leveling mechanism). Floated compasses are not suitable for MAV applications and magnetometer pairs cannot generate an accurate heading information unless the vehicle is level: a severe limitation for MAV applications. An algorithm more suited for General Aviation applications was developed in [1] because the algorithm ignores soft-iron errors. In General Aviation or larger aircraft applications, the issues of soft-iron errors are obviated by locating magnetometer in a part of the vehicle where these errors are not present.

Applying the algorithms in [13–15] directly to nonspace applications will not yield good results. This is because these algorithms require a measurement of Earth's magnetic field at various geographic locations. Earth's magnetic field changes slowly as a function of position, and although spacecraft (especially those in low Earth orbit) will traverse a large geographic range during the calibration process, this is an unreasonable requirement for vehicles like MAVs. Although the algorithms developed in [16–20] can be used in MAV applications, the unobservable error mode inherent in these calibration algorithms and its relation to soft-iron errors, which are important in miniature vehicle applications, was not fully discussed.

Paper Contributions

In view of the preceding paragraphs, this paper develops an autocalibration algorithm for a triad of magnetometers. The algorithm is similar to the ones developed in [16–20] in that it used Earth's magnetic field vector as a constraint. Although this leads to the same conditional observability problem all these algorithms share, the algorithm developed here has a method by which to identify when this condition occurs and when additional external information is needed to complete the calibration. The algorithm determines calibration parameters by fitting magnetometer data (collected from a vehicle executing a few precalibration turns or maneuvers) to an ellipsoid. It is different from the locus-constraint autocalibration algorithm presented in [1] in that it bypasses *some* of the observability problems by estimating a correction map instead of individual sensor errors. In addition, unlike the previous autocalibration algorithms in the same class, which use an iterative least-squares solution, the algorithm developed here uses a noniterative total least-squares estimator.

Paper Organization

This paper is organized in the following manner: First, a model for magnetometer output errors is presented. This is followed by an overview of the idea behind locus-constraint autocalibration of magnetometer pairs. The intent of the overview is to highlight the fact that the locus of magnetic field measurements from a triad of magnetometers is constrained to lie on an ellipsoid and how various magnetometer output errors affect this locus. Next, the details of the calibration algorithm proposed in this paper are discussed. This is followed by a discussion of the results from a series of simulations studies assessing the performance of the algorithm. Concluding remarks and suggestions for future work close the paper.

Magnetometer Error Model

Magnetometers used for heading determination in small aerial vehicles such as MAVs, unmanned aerial vehicles (UAVs), and General Aviation aircraft measure the intensity or strength of Earth's magnetic field vector $\boldsymbol{h}$. The sensing axes of the magnetometers will normally be aligned with the body axes of the vehicle. Thus, what the magnetometers pair measures are the components of $\boldsymbol{h}$ resolved along the body axes of the vehicle, or $\boldsymbol{h}^b$. The magnetometer measured or sensed magnetic field vector is denoted $\boldsymbol{h}^m$, where the superscript m indicates the vector is resolved along the measurement or sensor axes. Although in a calibrated or error-free magnetometer $\boldsymbol{h}^b = \boldsymbol{h}^m$, in practice sensor or installation errors lead to the situation in which $\boldsymbol{h} \neq \boldsymbol{h}^m$.

The purpose of calibration algorithms is to estimate a set of parameters that allow correcting the erroneous measured vector $\boldsymbol{h}^m$ so that it is equal to the true field vector $\boldsymbol{h}^b$. There are two ways to do this. The first way is to use an approach similar to the one in [1,22] where the actual sensor errors (which will be discussed in more detail later) causing $\boldsymbol{h}^b \neq \boldsymbol{h}^m$ are estimated. Subsequently, these error estimates are used to correct $\boldsymbol{h}^m$. In the second approach, instead of the actual sensor errors, a general mapping from $\boldsymbol{h}^m$ to $\boldsymbol{h}^b$ ($\boldsymbol{h}^m \mapsto \boldsymbol{h}^b$) is estimated [12–19]. Subsequently, each time a magnetometer measurement $\boldsymbol{h}^m$ is made, the map is used to correct $\boldsymbol{h}^m$ to be equal to $\boldsymbol{h}$. The algorithm developed in this paper takes the second approach and estimates $\boldsymbol{h}^m \mapsto \boldsymbol{h}^b$.

The $\boldsymbol{h}^m \mapsto \boldsymbol{h}^b$ mapping can be derived by noting that the measured field components are related to the error-free field values by the following matrix equation:

$$\boldsymbol{h}^m = \mathbf{C}\boldsymbol{h}^b + \boldsymbol{b} + \boldsymbol{n} \tag{1}$$

The matrix $\mathbf{C}$, which is the product of three separate matrices, is given by

$$\begin{aligned}\mathbf{C} &= \mathbf{C}_s\mathbf{C}_\eta\mathbf{C}_\alpha \\ &= \begin{bmatrix} 1+s_x & 0 & 0 \\ 0 & 1+s_y & 0 \\ 0 & 0 & 1+s_z \end{bmatrix} \begin{bmatrix} 1 & \eta_z & -\eta_y \\ -\eta_z & 1 & \eta_x \\ \eta_y & -\eta_x & 1 \end{bmatrix} \\ &\times \begin{bmatrix} 1+\alpha_{xx} & \alpha_{xy} & \alpha_{xz} \\ \alpha_{yx} & 1+\alpha_{yy} & \alpha_{yz} \\ \alpha_{zx} & \alpha_{zy} & 1+\alpha_{zz} \end{bmatrix}\end{aligned} \tag{2}$$

Null shifts or hard-iron biases are represented by the constant vector $\boldsymbol{b}$. The effect of wide band, sampling, or sensor noise (uncorrelated noise) is represented by the matrix $\boldsymbol{n}$. The matrix $\mathbf{C}_s$ represents the effect of scale factor errors where the parameters s_i ($i = x, y,$ or z) are the ith axes sensor's scale factor deviations. The $\mathbf{C}_s$ combined effect of soft irons and sensing axes nonorthogonality. Without loss of generality it can be written in terms of the magnetic induction coefficients, which give rise to the time-varying soft-iron errors. The notation α_{ij}, where i and j can be x, y, or z, is understood to be the proportionality constant (or induction coefficient), which relates the induced magnetic field in the body i direction resulting from of a field applied in the body j direction. Accordingly, $1 + \alpha_{ii}$ represents an

amplification or reduction of the field intensity along the i axes due to soft irons. Note that α_{ij} is not necessarily equal to α_{ji}. The *physical* misalignment between the measurement and body axes is represented by the transformation matrix $\mathbf{C}_\eta$, where η_x, η_y, and η_z are small rotations about the body x, y, and z axes, respectively. The autocalibration algorithm developed in [1] attempts to estimate each of the sensor error parameters (s_i, η_i, α_{ij}, b_i). As we will show later, this is not always possible in the context of locus-constraint algorithms. This is why in [1] some of these sensor error parameters were set equal to zero (η and α_{ij}) a priori.

The calibration of magnetometers is now reduced to determining parameters of the inverse of the mapping given by Eq. (1) or

$$\boldsymbol{h}^{\,b} = \mathbf{C}^{-1}\boldsymbol{h}^m - \mathbf{C}^{-1}\boldsymbol{b} - \mathbf{C}^{-1}\boldsymbol{n} = \mathbf{G}(\boldsymbol{h}^m - \boldsymbol{b}) - \mathbf{G}\boldsymbol{n} \tag{3}$$

This relationship will map erroneous magnetometer outputs into the correct (or true) measurement. This mapping is defined only if $\mathbf{C}$ is nonsingular. This is not an unreasonable assumption because a singular $\mathbf{C}$ would indicate 100% scale factor errors on all magnetometers ($s_x = s_y = s_z = -1$) or a singular $\mathbf{C}_\alpha$. These are unrealistic or pathological scenarios, and thus, without a loss of generality, we can assume that $\mathbf{C}^{-1}$ exists.

Locus-Constraint Autocalibration

Locus-constraint magnetometer autocalibration procedures such as the ones in [1,20,22] and the one developed in this paper rely on the fact that in a given geographical area, the magnitude of Earth's magnetic field vector $\boldsymbol{h}$, is a known constant and equal to $\sqrt{\boldsymbol{h}^T\boldsymbol{h}}$. This implies

$$\boldsymbol{h}^T\boldsymbol{h} = [\mathbf{G}(\boldsymbol{h}^m - \boldsymbol{b}) - \mathbf{G}\boldsymbol{n}]^T[\mathbf{G}(\boldsymbol{h}^m - \boldsymbol{b}) - \mathbf{G}\boldsymbol{n}] \tag{4}$$

$$= (\boldsymbol{h}^m)^T\Gamma\boldsymbol{h}^m - 2\boldsymbol{b}^T\Gamma\boldsymbol{h}^m + \boldsymbol{b}^T\Gamma\boldsymbol{b} + \tilde{\boldsymbol{n}} \tag{5}$$

where $\tilde{\boldsymbol{n}}$ represents the modified sensor noise term given by

$$\tilde{\boldsymbol{n}} = -2(\boldsymbol{h}^m - \boldsymbol{b})\mathbf{G}^T\mathbf{G}\boldsymbol{n} + \boldsymbol{n}^T\mathbf{G}^T\mathbf{G}\boldsymbol{n} \tag{6}$$

and Γ is the matrix given by

$$\Gamma = \mathbf{G}^T\mathbf{G} = \begin{bmatrix} \gamma_1 & \gamma_2 & \gamma_3 \\ \gamma_2 & \gamma_4 & \gamma_5 \\ \gamma_3 & \gamma_5 & \gamma_6 \end{bmatrix} \tag{7}$$

As shown in [1], the sampling noise $\boldsymbol{n}$ on the magnetometer output may be modeled as a zero-mean, Gaussian process. Even though $\boldsymbol{n}$ may be zero-mean and Gaussian, the modified sensor noise term $\tilde{\boldsymbol{n}}$ may not. This is because of the mapping of $\boldsymbol{n}$ through the term $-2(\boldsymbol{h}^m - \boldsymbol{b})\mathbf{G}^T\mathbf{G}$ term and the positive additive term $\boldsymbol{n}^T\mathbf{G}^T\mathbf{G}\boldsymbol{n}$. This, in part, leads us to selecting a total least-squares (TLS) estimator [26–28] for the calibration algorithm that will be discussed later in the paper.

Equation (5) is the equation of an ellipsoid or sphere in terms of $\boldsymbol{h}^m = [\,h_x^m \quad h_y^m \quad h_z^m\,]^T$. Because Eq. (5) indicates that the field measurements are constrained to lie on an ellipsoid, locus-constraint autocalibration algorithms estimate the entries of $\mathbf{G}$ and $\boldsymbol{b}$ by fitting an ellipsoid to measured magnetic field data. The relation between the entries of $\mathbf{G}$, $\boldsymbol{b}$, and the measured magnetic field data can be found by expanding Eq. (5). Given N magnetometer measurements, this relationship can be written as the following linear system of N equations:

$$\boldsymbol{r} = \mathbf{H}\xi \tag{8}$$

where $\boldsymbol{r} \in \mathbb{R}^{N\times 1}$ is a field residual vector (equal to zero for data collected from an error- and noise-free magnetometer triad) and $\xi \in \mathbb{R}^{10\times 1}$ is given by

$$\xi = [\,\gamma_1 \quad \gamma_2 \quad \gamma_3 \quad \cdots \quad \gamma_9 \quad \gamma_{10}\,]^T \tag{9}$$

The ith row of the linear system given by Eq. (8) is equal to

$$\begin{aligned} r_i = {} & \gamma_1\left(h_x^m\right)_i^2 + 2\gamma_2\left(h_x^m h_y^m\right)_i + 2\gamma_3\left(h_x^m h_z^m\right)_i \\ & + 2\gamma_4\left(h_y^m\right)_i^2 + 2\gamma_5\left(h_y^m h_z^m\right)_i + \gamma_6\left(h_z^m\right)_i^2 + \gamma_7\left(h_x^m\right)_i \\ & + \gamma_8\left(h_y^m\right)_i + \gamma_9\left(h_z^m\right)_i + \gamma_{10} \end{aligned} \tag{10}$$

where γ_1 through γ_6 are elements of the Γ matrix and

$$\gamma_7 = -2(\gamma_1 b_x + \gamma_2 b_y + \gamma_3 b_z) \tag{11}$$

$$\gamma_8 = -2(\gamma_2 b_x + \gamma_4 b_y + \gamma_5 b_z) \tag{12}$$

$$\gamma_9 = -2(\gamma_3 b_x + \gamma_5 b_y + \gamma_6 b_z) \tag{13}$$

$$\begin{aligned} \gamma_{10} = {} & \gamma_1 b_x^2 + 2\gamma_2 b_x b_y + 2\gamma_3 b_x b_z + \gamma_4 b_y^2 + 2\gamma_5 b_y b_z \\ & + 2\gamma_6 b_z^2 - \boldsymbol{h}^T\boldsymbol{h} \end{aligned} \tag{14}$$

The calibration algorithm involves solving for ξ using Eq. (8) and then using the values of γ_1 through γ_{10} to construct the affine mapping defined by $\mathbf{G}$ and $\boldsymbol{b}$ in Eq. (3).

Parameter Estimation

The autocalibration algorithm developed here proceeds in three steps. In the first step, a TLS [26–28] estimator is used to determine a normalized estimate of ξ denoted $\bar{\xi}$. That is, $\bar{\xi} = (\|\xi\|)^{-1}\xi$. The second step involves determining $\boldsymbol{b}$ and using this information to determine $\|\xi\|$. The value of $\|\xi\|$ is used to scale $\bar{\xi}$ such that it is equal to ξ. In the third step, the estimate of ξ is used to construct the $\mathbf{G}$ matrix. More precisely, ξ is used to construct the matrix $\mathbf{K}_G$, which is defined as

$$(\mathbf{K}_G) = (\mathbf{R}_G)^T\mathbf{G} \tag{15}$$

The matrix $\mathbf{K}_G$ is the symmetric scaling matrix obtained from the polar decomposition of $\mathbf{G}$. When $\mathbf{R}_G$ is the identity matrix, calibration of the magnetometer pair is complete after the third step. Whether the assumption that $\mathbf{R}_G$ is equal (or close) to the identity matrix is accurate or not can determined by examining the magnitude of the coefficients of the cross terms in ξ (i.e., γ_2, γ_3, and γ_5). If this assumption is not valid, it is an indication that there is an unobservable mode (or set of parameters) caused by soft-iron or sensor axes nonorthogonality. In this case, external information will be needed to estimate it and complete the calibration. If the vehicle is on the ground and in addition to the magnetometers, a triad of accelerometers and a GPS receiver are available, then the algorithm discussed in [29] can be used to estimate $\mathbf{R}_G$.

Determination of $\bar{\xi}$

In the first step of the calibration algorithm, an estimator is used to determine ξ by solving Eq. (8). An estimator is used because there are more data than unknowns (N measurements and 10 unknowns) and we want to use all available data optimally. If the magnetometer measurements were noiseless, Eq. (8) would be of the form $\mathbf{0} = \mathbf{H}\xi$. In the presence of noise, however, the left-hand side of this equation is nonzero. Because, in the error-free case, the left-hand side of Eq. (8) is equal to zero, the traditional least-squares estimator (or its stochastic derivatives such as the Kalman filter) would be inappropriate; they would yield the trivial solution $\xi = \mathbf{0}$. This pathology is due to, in part, the fact that both inputs to the problem (h_x^m h_y^m and h_z^m) are corrupted by noise, and the measurement matrix $\mathbf{H}$ is a function of these corrupted measurements. A reasonable estimator would be one that provides an optimal estimate of ξ (denoted $\hat{\xi}$) such that the sum of the squares of the residuals are minimized. Mathematically, this can be written as

$$\hat{\xi} = \min_{\xi} \|\boldsymbol{r}\|_2 = \min_{\xi} (\xi^T \mathbf{H}^T \mathbf{H} \xi) \tag{16}$$

with the constraint that $\xi \neq \mathbf{0}$. We can readily see the solution to this problem if we use a singular value decomposition (SVD) to rewrite $\mathbf{H}^T\mathbf{H}$ as

$$\mathbf{H}^T\mathbf{H} = \mathbf{V}_H \Sigma_H^2 \mathbf{V}_H^T \tag{17}$$

Equation (16) would be minimized if $\hat{\xi} = \boldsymbol{v}_{10}$, where $\boldsymbol{v}_{10}$ is the tenth column of $\mathbf{V}_H$ or the eigenvector associated with the smallest singular value of $\mathbf{H}$. However, $\|\boldsymbol{v}_{10}\| = 1$, so the estimate obtained from the SVD of $\mathbf{H}$ is

$$\boldsymbol{v}_{10} = \frac{\xi}{\|\xi\|} \tag{18}$$

We will denote this normalized estimate of ξ as $\bar{\xi}$ and use it to determine $\boldsymbol{b}$. Once b is known, $\bar{\xi}$ can be scaled up to ξ. Before we proceed with the estimation of $\boldsymbol{b}$, however, we note that the solution of Eq. (8) given by optimization defined in Eq. (16) is what is known as the TLS estimate of ξ [26–28]. Even though it is not apparent from the earlier development, the TLS estimate not only minimizes Eq. (16) but also provides an estimate of a matrix $\boldsymbol{\Delta}\mathbf{H}$ that corrects the noise-corrupted columns of $\mathbf{H}$ via the following cost function:

$$\boldsymbol{\Delta}\mathbf{H} = \min_{\boldsymbol{\Delta}\mathbf{H}} \|\mathbf{H} - \boldsymbol{\Delta}\mathbf{H}\|_F \tag{19}$$

The sensor noise $\boldsymbol{n}$ and the modified sensor noise term $\tilde{\boldsymbol{n}}$ discussed in association with Eq. (5) corrupt the columns of $\mathbf{H}$. Thus, the TLS solution adjusts both the column and row space of $\mathbf{H}$ in deriving an optimal solution for Eq. (8).

Determination of b and Scaling $\bar{\xi}$

Examining Eqs. (7) and (11–13) shows that once ξ is estimated, the elements of $\boldsymbol{b}$ can be extracted independently of the elements of $\mathbf{K}_G$. However, at this point all we have is $\bar{\xi}$ and not ξ. Fortunately, the norm of ξ does not affect the estimation of $\boldsymbol{b}$. We can see this if we rearrange Eqs. (11–13) to solve for $\boldsymbol{b}$ as follows:

$$\boldsymbol{b} = -\frac{1}{2}\begin{bmatrix} \gamma_1 & \gamma_2 & \gamma_3 \\ \gamma_2 & \gamma_4 & \gamma_5 \\ \gamma_3 & \gamma_5 & \gamma_6 \end{bmatrix}^{-1} \begin{bmatrix} \gamma_7 \\ \gamma_8 \\ \gamma_9 \end{bmatrix} \tag{20}$$

Examining Eq. (20), we see that scaling all the γ_i values by the same amount does not affect the estimate of $\boldsymbol{b}$. Thus, we can solve for $\boldsymbol{b}$ using Eq. (20), where instead of γ_i (or the elements of the vector ξ) we use $\bar{\gamma}_i$ (the elements of the vector $\bar{\xi}$). Once $\boldsymbol{b}$ has been determined, we can scale $\bar{\xi}$ to ξ using Eq. (14). This is possible because $\|\boldsymbol{h}\| = \boldsymbol{h}^T\boldsymbol{h}$ is a known quantity. It is the magnitude of Earth's magnetic field vector in a given geographical area and can be computed using the model in [11]. Thus, we can determine $\|\xi\|$ by rearranging Eq. (14) as follows:

$$\|\xi\| = \boldsymbol{h}^T\boldsymbol{h}\Big(\bar{\gamma}_1 b_x^2 + 2\bar{\gamma}_2 b_x b_y + 2\bar{\gamma}_3 b_x b_z + \bar{\gamma}_4 b_y^2 + 2\bar{\gamma}_5 b_y b_z + 2\bar{\gamma}_6 b_z^2 - \bar{\gamma}_{10}\Big)^{-1} \tag{21}$$

Using this result we construct the final value of $\xi = (\|\xi\|)\bar{\xi}$.

Determining $\mathbf{K}_G$

From Eq. (7) we note that $\boldsymbol{\Gamma}$ and $\mathbf{G}$ have the same left eigenvectors. Also, the singular values of $\mathbf{G}$ are equal to the square root of the singular values of $\boldsymbol{\Gamma}$. Thus, an eigenvalue/eigenvector decomposition of $\boldsymbol{\Gamma}$ allows us to construct $\mathbf{K}_G$ as follows:

$$\mathbf{K}_G = \mathbf{V}_\Gamma \sqrt{\Sigma_\Gamma} \mathbf{V}_\Gamma^T \tag{22}$$

Using Eqs. (3) and (20) we can write the complete calibration solution (or $\boldsymbol{h}^m \mapsto \boldsymbol{h}$) as follows:

$$\boldsymbol{h} = \mathbf{R}_G\Big(\mathbf{V}_\Gamma \sqrt{\Sigma_\Gamma} \mathbf{V}_\Gamma^T\Big)\left(\boldsymbol{h}^m + \frac{1}{2}\begin{bmatrix} \gamma_1 & \gamma_2 & \gamma_3 \\ \gamma_2 & \gamma_4 & \gamma_5 \\ \gamma_3 & \gamma_5 & \gamma_6 \end{bmatrix}^{-1} \begin{bmatrix} \gamma_7 \\ \gamma_8 \\ \gamma_9 \end{bmatrix}\right) \tag{23}$$

Of course, if $\mathbf{R}_G$ is not the identity matrix, it will need to be estimated using external sensor information. The matrix $\mathbf{R}_G$ is the identify when soft-iron errors are not present or negligible, and, in which case, Eq. (23) represents the complete calibration solution.

Note that the solution given by Eq. (23) represents the solution to the problem of fitting an ellipsoid to noisy measurement data. This problem is not new and has been dealt with in computer graphics [30,31], medical imaging [32], and other applications [33]. There is a difference, however, in that unlike the problems discussed in [30–33], the ellipsoid problem here has additional degrees of freedom arising from nonorthogonality of the measurement axes, which is either physical or apparent due to soft-iron errors.

Algorithm Performance

In what follows, simulation results that highlight the performance of the autocalibration algorithm developed in this paper are presented. In particular, the effect of the *apparent* nonorthogonality and misalignment caused by soft iron will be evaluated. This will be shown by considering the calibration of a magnetometer triad in two different installations, where the output of the sensor is corrupted by the errors listed in Table 1. As can be seen from Table 1, the difference between the two installations is that in case 2 the magnetometers are affected by soft-iron errors.

If we assume that the total measurement locus shown in Fig. 1 is used in the calibration algorithm, this leads to the results shown in Figs. 2 and 3. These figures show the 2-D loci of magnetic field measurements. The dark-colored contours represent the true locus, and the light-color contours represent the outputs of the magnetometer triad after the estimated $\boldsymbol{h}^m \mapsto \boldsymbol{h}^b$ map defined by Eq. (23) is applied. Comparing these two figures, we note that there is a complete overlap between the true and postcalibration measured contours for case 1, whereas there remains an apparent misalignment for case 2. For case 2, the true $\mathbf{G}$ matrix and its polar decomposition are given by

$$\mathbf{G} = \mathbf{R}_G\mathbf{K}_G = \begin{bmatrix} 0.9976 & 0.0672 & -0.0186 \\ -0.0676 & 0.9975 & -0.0224 \\ 0.0170 & 0.0236 & 0.9996 \end{bmatrix} \times \begin{bmatrix} 0.8807 & -0.1875 & -0.0962 \\ -0.1875 & 1.1374 & -0.0183 \\ -0.0962 & -0.0183 & 0.5814 \end{bmatrix} \tag{24}$$

Table 1 Errors assumed in the simulation studies

Error parameter	Case 1	Case 2
b_x	−0.12 Gauss	−0.12 Gauss
b_y	0.17 Gauss	0.17 Gauss
b_z	−0.26 Gauss	−0.26 Gauss
η_i	0 deg	0.00 deg
α_{xx}	0	0.05
α_{xy}	0	0.10
α_{xz}	0	0.20
α_{yx}	0	0.30
α_{yy}	0	0.03
α_{yz}	0	0.20
α_{zx}	0	0.01
α_{zy}	0	0.20
α_{zz}	0	1.0
s_x	0.15	0.15
s_y	−0.13	−0.13
s_z	−0.12	−0.12
$n_x = n_y$	0.001 Gauss	0.001 Gauss

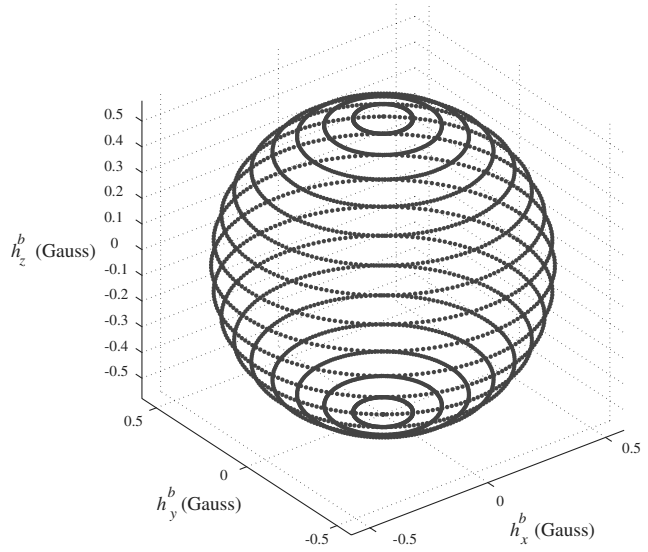

Fig. 1 Measurement locus of Earth's magnetic field at geographical coordinates: N44.9° latitude, E93.2° longitude and 256 m above mean sea level (MSL).

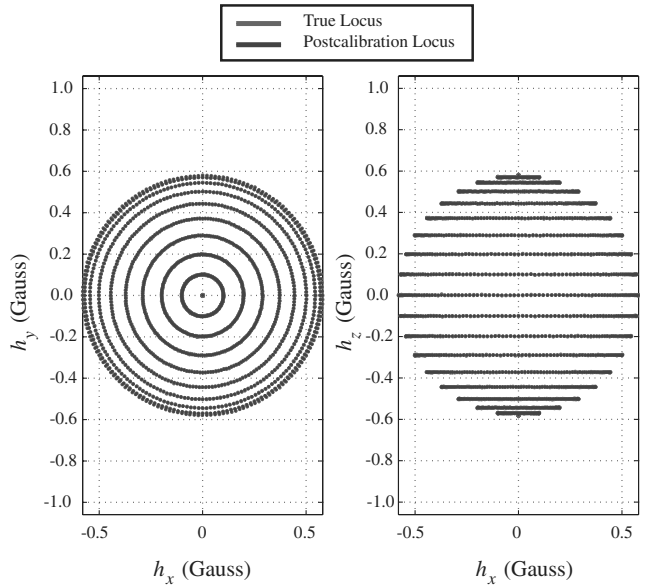

Fig. 2 Case 1: comparison of true field and estimated field after correction map is applied.

The value of $\mathbf{K}_G$ estimated by the algorithm (denoted $\hat{\mathbf{K}}_G$) is given by

$$\hat{\mathbf{K}}_G = \begin{bmatrix} 0.8807 & -0.1875 & -0.0961 \\ -0.1875 & 1.1372 & -0.0183 \\ -0.0961 & -0.0183 & 0.5814 \end{bmatrix} \tag{25}$$

The difference between $\hat{\mathbf{K}}_G$ and $\mathbf{K}_G$ is seen to be very small. Thus, the primary difference between the postcalibration magnetometer outputs and the true field measurement will be an *apparent* misalignment due to soft irons captured by the orthogonal matrix $\mathbf{R}_G$. To get a better sense of the magnitude of this error, we can express it in terms of an equivalent *physical* misalignment $\mathbf{C}_\eta$. This equivalence of $\mathbf{C}_\eta$ and $\mathbf{C}_\alpha$ is shown in Fig. 4, which is a simplified schematic of a 2-D calibration problem. What is apparent from this schematic is that there can be a family of matrices $\mathbf{C}'_\alpha$ and $\mathbf{C}'_\eta$ whose effect on the magnetometer triad output is identical and indistinguishable from observing outputs only. Thus, if we assume that η_z, η_y, and η_x are the 3-2-1 Euler angle sequences of the rotation between the b and m frames, respectively, then $\mathbf{R}_G$ in simulation

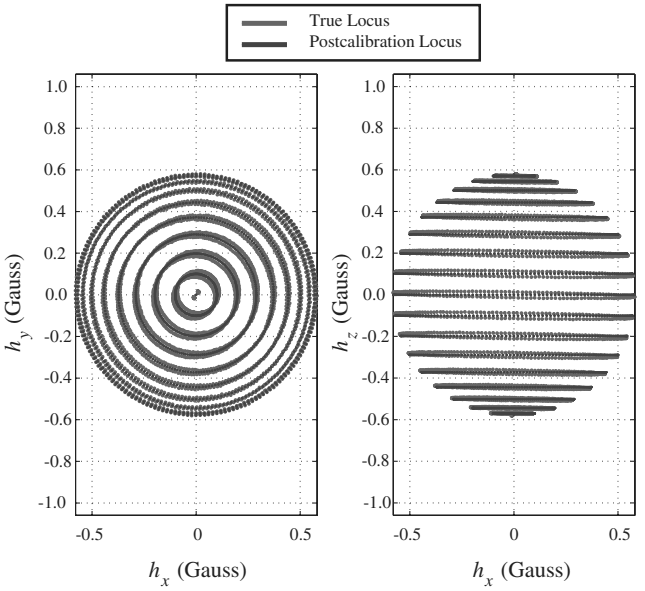

Fig. 3 Case 2: comparison of true field and estimated field after correction map is applied.

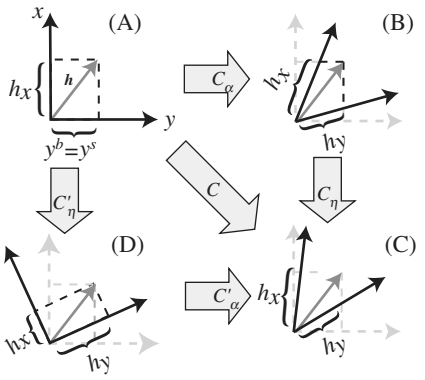

Fig. 4 Action of error matrix $\mathbf{C} = \mathbf{G}^{-1}$.

case 2 is equivalent to the following rotations:

$$\eta_z = 3.8535 \text{ deg} \qquad \eta_y = 1.0636 \text{ deg} \qquad \eta_x = -1.2817 \text{ deg} \tag{26}$$

The effect of $\mathbf{R}_G$ can be significant even when the equivalent rotations are as small as those in the case 2 example. This can be seen if we consider the simulated flight trajectory shown in Fig. 5 and the associated attitude history shown in Fig. 6. If magnetometers in case 1 and case 2 were calibrated using the autocalibration algorithm developed in this paper and then used for heading determination along the trajectory shown in Fig. 5, the heading history and errors shown in Fig. result. In the case of no soft-iron effects (case 1), the autocalibration algorithm results in heading residuals that are small. However, the heading errors resulting from neglecting soft-iron effects in case 2 can be as large as 10 deg.

It should be noted that the complete locus ellipsoid is difficult to obtain in practice. This is because it requires that the vehicle span the entire Euler angle attitude space. However, MAV can be easily moved around by hand, and thus, it is easy to obtain a partial ellipse as shown in Fig. 8. The locus shown in Fig. 8 results from taking a few samples of measurements as the vehicle is moved ± 85 deg in pitch and ± 90 deg in roll. The results of the calibration using this locus are also shown in Fig. 7 and are very similar to the results obtained using the full locus.

The estimates of γ_2, γ_3, γ_5 will be nonzero if $\mathbf{R}_G \neq \mathbf{I}$ and equal to zero when $\mathbf{R}_G = \mathbf{I}$. However, because of the measurement noise vector $\boldsymbol{n}$, they will never be identically zero. A threshold based on the

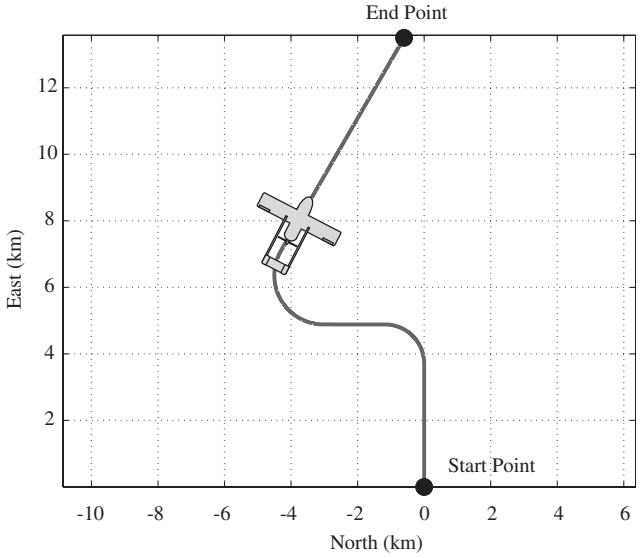

Fig. 5 Simulated vehicle trajectory.

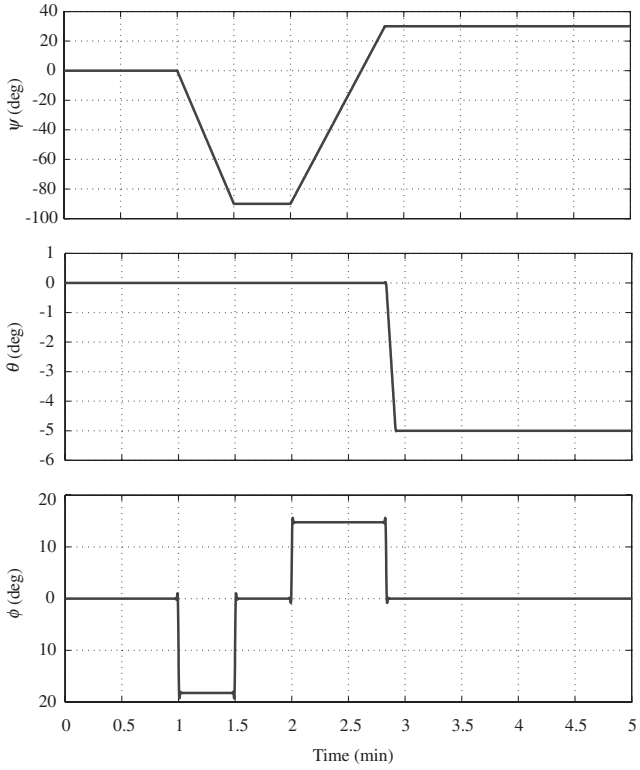

Fig. 6 Attitude history corresponding to vehicle trajectory shown in Fig. 5.

magnitude of $\boldsymbol{n}$ can be established to determine when they are nonzero. If the values of these parameters are larger than this threshold, then it is an indication that $\mathbf{R}_G$ is not the identity or close to the identity matrix, and soft-iron errors are important. This can be seen in Fig. 9, in which the estimates of these parameters for 10,000 simulation runs are shown. Clearly, the estimates for case 1 are zero mean, whereas the case 2 values are biased away from zero. Because the 1σ value of the sensor wide band noise for this case is 0.001 Gauss (a typical value for a sensor of the class used in MAV applications [34]), a threshold larger than the noise value can be used to discriminate between the cases in which soft-iron errors are important and those cases in which they are not important.

To be on the conservative side, one may elect to always assume that $\mathbf{R}_G$ is not the identity matrix and estimate the rotations that

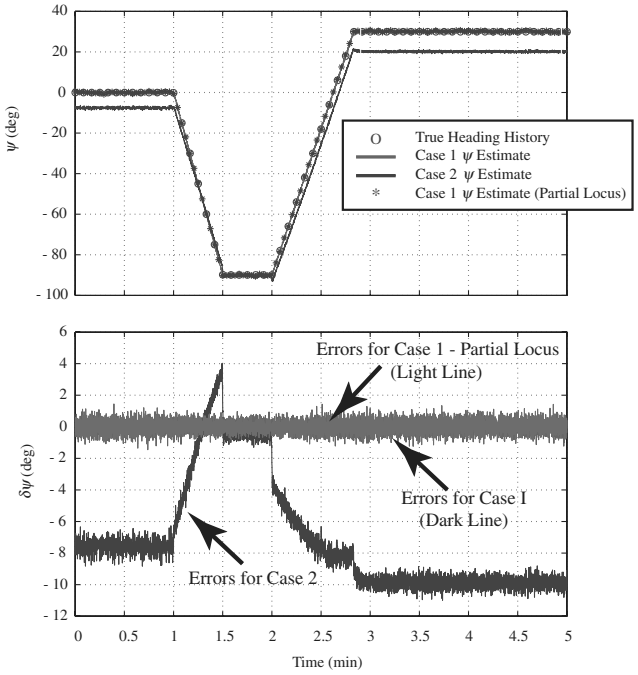

Fig. 7 Postcalibration heading estimate and heading estimation error history.

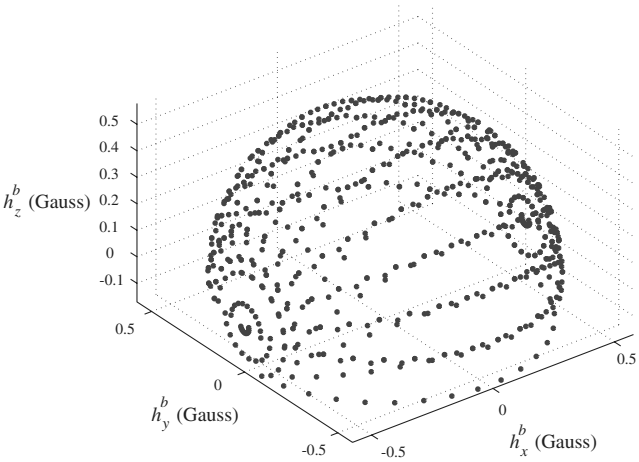

Fig. 8 Realistic field measurement locus for MAV applications.

constitute it using external information while the vehicle is on the ground. This can be done by using a vector matching attitude determination algorithm similar to the one presented in [29]. In this case, the two vectors that would be used are at least two measurements of $\boldsymbol{h}$ at different headings. It is worth noting that even in this case the information provided by the magnitudes of γ_2, γ_3, and γ_5 is useful. Even if we always assume $\mathbf{R}_G$ is the identity and estimate the rotations that constitute the matrix, the magnitude of these parameters can be used as means by which an assessment of whether a given location where magnetometers are installed is free from soft-iron errors.

Conclusions

This paper presented an autocalibration algorithm for magnetometer triads that leveraged the field measurement locus constraint. It was shown that in some instances a locus-constraint calibration algorithm will be unobservable. Errors due to soft iron are indistinguishable from errors due to *physical* nonorthogonality or misalignments. In the presence of soft-iron errors, locus-constraint autocalibration algorithms can only provide 9 of the 12 calibration parameters. The remaining three parameters will be the *apparent*

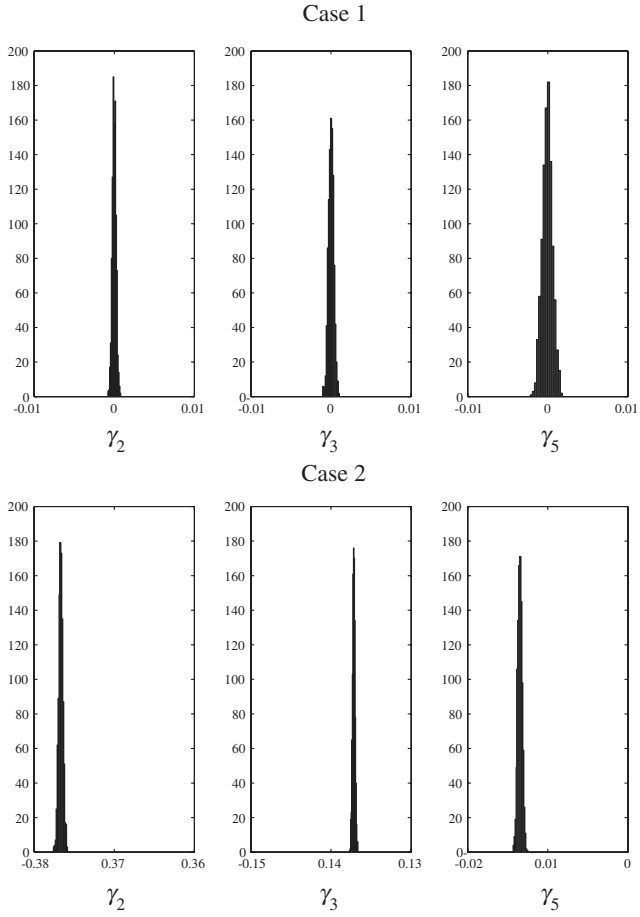

Fig. 9 Histogram of γ_2, γ_3, and γ_5 for 10,000 simulation runs using the locus shown in Fig. 8.

rotations that define $\mathbf{R}_G$. This is of paramount importance in MAV applications where size constraints may require locating magnetometers close to soft-iron material. If not accounted for, these errors can lead to large heading errors. Although the complete effect of these errors is not observable from autocalibration, the unobservable errors can be dealt with by introducing external sensor information. The information needed can be obtained using velocity measurements from a GPS receiver and leveling information from a triad of accelerometers during the calibration process.

Acknowledgment

The author gratefully acknowledges the support of the Intelligent Transportation Systems (ITS) Institute at the University of Minnesota and the U.S. Air Force Office of Scientific Research for the grants that supported this work. The results and views expressed in this paper, however, belong to the author alone and do not necessarily represent the position of any other organization or person.

References

[1] Gebre-Egziabher, D., Elkaim, G. H., Powell, J. D., and Parkinson, B. W., "Calibration of Strapdown Magnetometers in the Magnetic Field Domain," *Journal of Aerospace Engineering*, Vol. 19, No. 2, 2006, pp. 87–102.

[2] Kayton, M., and Fried, W., *Avionics Navigation Systems*, 2nd ed., John Wiley and Sons, New York, 1997, pp. 436–447.

[3] Winkler, S., Buschmann, M., and Vörsmann, P., "Designing the Worlds Smallest Integrated Navigation System for Micro Aerial Vehicles," *Inside GNSS*, Vol. 2, No. 1, 2007, pp. 44–51.

[4] Bar-Itzhack, I. Y., and Berman, N., "Control Theoretic Approach to Inertial Navigation Systems," *Journal of Guidance, Control, and Dynamics*, Vol. 11, No. 3, 1988, pp. 237–245.

[5] Goshen-Meskin, D., and Bar-Itzhack, I. Y., "Observability Analysis of Piece-Wise Constant Systems—Part 1: Theory," *IEEE Transactions on Aerospace and Electronic Systems*, Vol. 28, No. 4, 1992, pp. 1065–1067.

[6] Goshen-Meskin, D., and Bar-Itzhack, I. Y., "Observability Analysis of Piece-Wise Constant Systems—Part 2: Application to Inertial Navigation In-Flight Alignment," *IEEE Transactions on Aerospace and Electronic Systems*, Vol. 28, No. 4, 1992, pp. 1068–1075.

[7] Rhee, I., Abdel-Hafez, M., and Speyer, J., "Observability of Integrated GPS/INS During Manuevers," *IEEE Transactions on Aerospace and Electronic Systems*, Vol. 40, No. 2, 2004, pp. 526–535.

[8] Shao, Y., and Gebre-Egziabher, D., "Stochastic and Geometric Observability of Aided Inertial Navigators," *Proceedings of the ION-GNSS Conference*, Institute of Navigation, Alexandria, VA, Sept. 2006, pp. 2723–2732.

[9] Wenger, L., "An Integrated INS/GPS System for an Autonomous Micro Air Vehicle," M.S. Thesis, ETH-Zürich, Zurich, May 2003.

[10] Wenger, L., and Gebre-Egziabher, D., "System Concepts and Observability Analysis of Multi-Sensor Navigation Systems for UAV Applications," AIAA Paper 2003-6647, Sept. 2003.

[11] Barton, C. E., "International Geomagnetic Reference Field: The Seventh Generation," *Journal of Geomagnetisim and Geoelectricity*, Vol. 49, No. 2, 1997, pp. 123–148.

[12] Lerner, G. M., and Shuster, M. D., "In-Flight Magnetometer Calibration and Attitude Determination for Near-Earth Spacecraft," *Journal of Guidance and Control*, Vol. 4, No. 5, 1981, pp. 518–522.

[13] Alonso, R., and Shuster, M. D., "TWOSTEP: A Fast Robust Algorithm for Attitude-Independent Magnetometer-Bias Determination," *Journal of the Astronautical Sciences*, Vol. 50, No. 4, 2002, pp. 433–451.

[14] Alonso, R., and Shuster, M. D., "Centering and Observability in Attitude-Independent Magnetometery Bias Determination," *Journal of the Astronautical Sciences*, Vol. 51, No. 2, 2003, pp. 133–141.

[15] Alonso, R., and Shuster, M. D., "Attitude-Independent Magnetometer-Bias Determination: A Survey," *Journal of the Astronautical Sciences*, Vol. 50, No. 4, 2002, pp. 453–475.

[16] Graven, P., and Kenny, T., "Laboratory (and On-Orbit) Magnetometer Calibration Without a Coil Facility of Orientation Information," *Proceedings of the Tenth Annual AIAA/USU Small Satellite Conference*, Utah State Univ., Logan, UT, Sept. 1996.

[17] Merayo, J. M. G., Brauer, P., Primdahl, F., and Petersen, J. R., "Absolute Calibration and Alignment of Vector Magnetometers in the Earth's Field," ESA Paper SP-490, 2002.

[18] Merayo, J. M. G., Brauer, P., Primdahl, F., and Petersen, J. R., and Nielsen, O. V., "Scalar Calibration of Vector Magnetometers," *Measurement Science and Technology*, Vol. 11, No. 2, 2000, pp. 120–132.

[19] Brauer, P., Merayo, J. M. G., Risbo, T., and Primdahl, F., "Magnetic Calibration of Vector Magnetometers: Linearity, Thermal Effects and Stability," ESA Paper SP-490, 2002.

[20] Hu, X., Liu, Y., Wang, Y., Hu, Y., and Yan, D., "Auto-Calibration of Electronic Compass for Augmented Reality," *Proceedings of the IEEE International Symposium on Mixed and Augmented Reality, ISMAR 2005*, IEEE, Piscataway, NJ, 2005, pp. 182–183.

[21] Hoff, B., and Azuma, R., "Auto-Calibration of an Electronic Compass in an Outdoor Augmented Reality System," *Proceedings of the IEEE and ACM International Symposium on Augmented Reality*, IEEE, Piscataway, NJ, 2000, pp. 159–164.

[22] Caruso, M. J., "Application of Magnetic Sensors for Low Cost Compass Systems," *Proceedings of the IEEE Position Location and Navigation Symposium, PLANS 2000*, IEEE, Piscataway, NJ, 2000, pp. 177–184.

[23] LITEF Corporation, LCR-92 Attitude Heading Reference System, LITEF Corporatoin, Freiberg, Germany, 2001.

[24] Bowditch, N., *The American Practical Navigator*, Defense Mapping Agency, Hydrographic/Topographic Center, Bethesda, MD, 1995, pp. 201–295.

[25] Hine, A., *Magnetic Compasses and Magnetometers*, Adam Hilger, London, 1968.

[26] van Huffel, S., and Vandewalle, J., "Analysis and Properties of the Generalized Total Least Squares Problem $\mathbf{AX} = \mathbf{B}$ when Some or All Columns are Subject to Error," *SIAM Journal on Matrix Analysis and Applications*, Vol. 10, No. 3, 1989, pp. 294–315.

[27] Golub, G. H., and van Loan, C. F., "An Analysis of Total Least Squares Problem," *SIAM Journal on Numerical Analysis*, Vol. 17, No. 6, 1980, pp. 883–893.

[28] Mühlich, M., and Mester, R., "The Role of Total Least Squares in Motion Analysis," *Proceedings of the European Conference on Computer Vision, 1998 (ECCV '98)*, Springer–Verlag, New York, 1998, pp. 305–321.

[29] Gebre-Egziabher, D., Elkaim, G. H., Powell, J. D., and Parkinson, B. W., "A Gyro-Free Quaternion Based Attitude Determination System Suitable for Implementation Using Low-Cost Sensors," *Proceedings of the IEEE PLANS 2002*, IEEE, Piscataway, NJ, 2002, pp. 185–192.

[30] O'Leary, P., and Zsombor-Murray, P., "Direct and Specific Least-Square Fitting of Hyperbolae and Ellipses," *Journal of Electronic Imaging*, Vol. 13, No. 3, 2004, pp. 492–503.

[31] Eberly, D., *3D Game Engine Design: A Practical Approach to Real-Time Computer Graphics*, Morgan Kaufmann, San Francisco, CA, 2001.

[32] Lin, X., Klette, G., Klette, R., Craig, J., and Simon, D., "Accurately Measuring the Size of the Pupil of the Eye," *Proceedings of Image and Vision Computing '03 Conference*, Massey Univ., Palmerston North, New Zealand, 2003, pp. 221–226.

[33] Gander, W., Golub, G. H., and Strebel, R., "Least-Squares Fitting of Circles and Ellipses," *BIT*, Vol. 34, No. 4, 1994, pp. 558–578.

[34] "Specification Sheet for HMR2300r:Three Axis Strapdown Magnetometer," Honeywell International Inc., Document 900232, Rev. B., Morristown, NJ, 1999.